



**HAL**  
open science

## Validation of proton dose calculation on scatter corrected 4D cone beam computed tomography using a porcine lung phantom

Henning Peter Schmitz, Moritz Rabe, Guillaume Janssens, David Bondesson, Simon Rit, Katia Parodi, Claus Belka, Julien Dinkel, Christopher Kurz, Florian Kamp, et al.

### ► To cite this version:

Henning Peter Schmitz, Moritz Rabe, Guillaume Janssens, David Bondesson, Simon Rit, et al.. Validation of proton dose calculation on scatter corrected 4D cone beam computed tomography using a porcine lung phantom. *Physics in Medicine and Biology*, 2021, 66 (17), pp.175022. 10.1088/1361-6560/ac16e9 . hal-03328275v2

**HAL Id: hal-03328275**

**<https://hal.science/hal-03328275v2>**

Submitted on 2 Sep 2021

**HAL** is a multi-disciplinary open access archive for the deposit and dissemination of scientific research documents, whether they are published or not. The documents may come from teaching and research institutions in France or abroad, or from public or private research centers.

L'archive ouverte pluridisciplinaire **HAL**, est destinée au dépôt et à la diffusion de documents scientifiques de niveau recherche, publiés ou non, émanant des établissements d'enseignement et de recherche français ou étrangers, des laboratoires publics ou privés.



## PAPER

## Validation of proton dose calculation on scatter corrected 4D cone beam computed tomography using a porcine lung phantom

## OPEN ACCESS

RECEIVED  
6 May 2021REVISED  
7 July 2021ACCEPTED FOR PUBLICATION  
22 July 2021PUBLISHED  
30 August 2021

Original content from this work may be used under the terms of the [Creative Commons Attribution 4.0 licence](#).

Any further distribution of this work must maintain attribution to the author(s) and the title of the work, journal citation and DOI.



Henning Schmitz<sup>1</sup> , Moritz Rabe<sup>1</sup> , Guillaume Janssens<sup>2</sup> , David Bondesson<sup>3</sup> , Simon Rit<sup>4</sup>,  
Katia Parodi<sup>5</sup> , Claus Belka<sup>1,6</sup>, Julien Dinkel<sup>3</sup>, Christopher Kurz<sup>1,5</sup>, Florian Kamp<sup>1,7,8</sup> and  
Guillaume Landry<sup>1,5,8</sup> 

<sup>1</sup> Department of Radiation Oncology, University Hospital, LMU Munich, Munich, Germany

<sup>2</sup> Ion Beam Applications SA, Louvain-la-neuve, Belgium

<sup>3</sup> Department of Radiology, University Hospital, LMU Munich, Munich, Germany

<sup>4</sup> Univ Lyon, INSA-Lyon, Université Claude Bernard Lyon 1, UJM-Saint Etienne, CNRS, Inserm, CREATIS UMR 5220, U1206, F-69373, LYON, France

<sup>5</sup> Department of Medical Physics, Faculty of Physics, Ludwig-Maximilians-Universität München (LMU Munich), Garching (Munich), Germany

<sup>6</sup> German Cancer Consortium (DKTK), Partner Site Munich, Munich, Germany

<sup>7</sup> Department of Radiation Oncology, University Hospital Cologne, Cologne, Germany

<sup>8</sup> These authors contributed equally.

E-mail: [henning.schmitz@med.uni-muenchen.de](mailto:henning.schmitz@med.uni-muenchen.de)

**Keywords:** 4DCBCT, proton therapy, lung cancer, lung phantom, scatter correction, adaptive radiotherapy, motion management

Supplementary material for this article is available [online](#)

## Abstract

Proton therapy treatment for lungs remains challenging as images enabling the detection of inter- and intra-fractional motion, which could be used for proton dose adaptation, are not readily available. 4D computed tomography (4DCT) provides high image quality but is rarely available in-room, while in-room 4D cone beam computed tomography (4DCBCT) suffers from image quality limitations stemming mostly from scatter detection. This study investigated the feasibility of using virtual 4D computed tomography (4DvCT) as a prior for a phase-per-phase scatter correction algorithm yielding a 4D scatter corrected cone beam computed tomography image (4DCBCT<sub>cor</sub>), which can be used for proton dose calculation. 4DCT and 4DCBCT scans of a porcine lung phantom, which generated reproducible ventilation, were acquired with matching breathing patterns. Diffeomorphic Morphons, a deformable image registration algorithm, was used to register the mid-position 4DCT to the mid-position 4DCBCT and yield a 4DvCT. The 4DCBCT was reconstructed using motion-aware reconstruction based on spatial and temporal regularization (MA-ROOSTER). Successively for each phase, digitally reconstructed radiographs of the 4DvCT, simulated without scatter, were exploited to correct scatter in the corresponding CBCT projections. The 4DCBCT<sub>cor</sub> was then reconstructed with MA-ROOSTER using the corrected CBCT projections and the same settings and deformation vector fields as those already used for reconstructing the 4DCBCT. The 4DCBCT<sub>cor</sub> and the 4DvCT were evaluated phase-by-phase, performing proton dose calculations and comparison to those of a ground truth 4DCT by means of dose-volume-histograms (DVH) and gamma pass-rates (PR). For accumulated doses, DVH parameters deviated by at most 1.7% in the 4DvCT and 2.0% in the 4DCBCT<sub>cor</sub> case. The gamma PR for a (2%, 2 mm) criterion with 10% threshold were at least 93.2% (4DvCT) and 94.2% (4DCBCT<sub>cor</sub>), respectively. The 4DCBCT<sub>cor</sub> technique enabled accurate proton dose calculation, which indicates the potential for applicability to clinical 4DCBCT scans.

## 1. Introduction

Proton therapy (PT) offers a ballistic advantage over photon therapy as there is considerably less energy deposition along the trajectory to the target and a negligible amount beyond, due to the complete stopping of

protons in matter at therapeutic energies. This localised energy release allows significant dose sparing in organs at risk (OAR) and a reduced integral dose. In modern PT facilities, the dose distribution can be shaped to improve dose conformity using pencil-beam scanned intensity-modulated proton therapy (IMPT) (Lomax *et al* 2001, 2004). Protons are used for treatment of different tumour entities such as head and neck (H&N) (Manzar *et al* 2020), oesophageal (Welsh *et al* 2011), paediatric brain (Lin *et al* 2020), gastrointestinal (Verma *et al* 2016), meningioma (Weber *et al* 2012), and non-small-cell lung carcinoma (NSCLC) (Nakajima *et al* 2018). PT may also be helpful in treatment-related complications (Kim *et al* 2019).

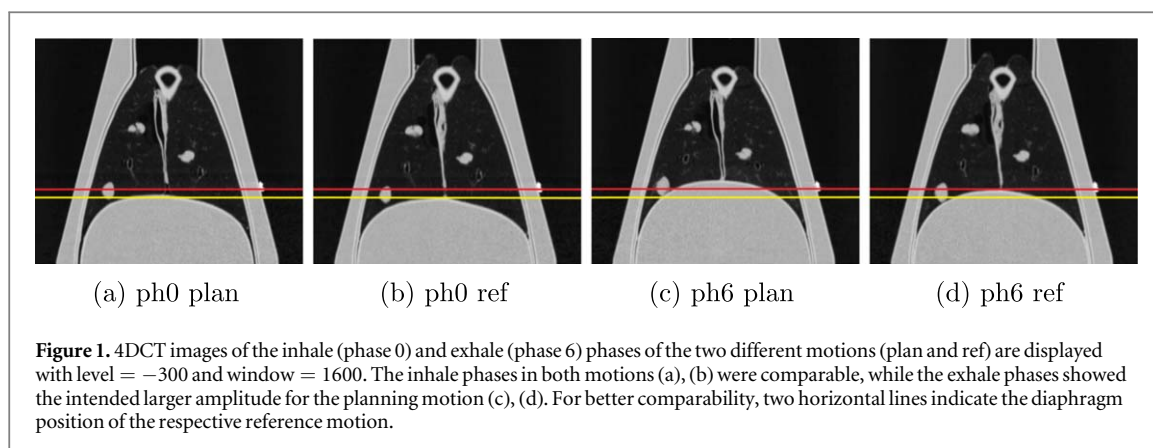
One drawback of PT is its high sensitivity to anatomical changes (Chen *et al* 2020b), which may occur during treatment, and which are typically classified as either inter- or intra-fractional. Inter-fractional changes include anatomical changes such as weight loss, stochastic motion of internal organs on a time scale of hours or more, and changes in tumour size. The second group contains respiratory and cardiac motion as well as the filling of bladder and bowel and is particularly relevant for tumours within the abdominothoracic region (Keall *et al* 2006). The characteristic Bragg-peak of charged particles makes PT very susceptible to these changes, which can compromise both target coverage and OAR sparing (Berman *et al* 2015). Respiration patterns can vary markedly between different fractions (McClelland *et al* 2010, Zhang *et al* 2015), and hence, for the treatment of moving tumours in the lung, it is of paramount importance to have daily 4D imaging. This would enable the detection of those variations and ideally allow their correction with treatment adaptation (Hoffmann *et al* 2017, Jakobi *et al* 2017, Tseng *et al* 2018, Albertini *et al* 2020), so that the full potential of IMPT can be exploited. Consequently, daily dose reconstructions including the geometry and breathing curve of the day are highly desired, but not yet accessible in clinical practice. Current approaches rely on weekly 4D computed tomography (4DCT) acquisitions and offline adaptations (Meijers *et al* 2020a). It would thus be beneficial to use cone beam computed tomography (CBCT) images, which are routinely acquired in the scope of image-guided PT for patient positioning, to reconstruct the delivered fraction dose.

While the CBCTs acquired for patient alignment show the anatomy of the day in treatment position, they cannot be used directly for proton dose calculation due to inaccurate CT numbers. Utilising CBCT scans (Rit *et al* 2016, Veiga *et al* 2016, Landry and Hua 2018) for proton dose calculation has seen considerable interest for anatomical sites unaffected by respiratory motion (Kurz *et al* 2015, Landry *et al* 2015, Veiga *et al* 2016, Thummerer *et al* 2020, Lalonde *et al* 2020), as it further offers the benefit of neither increasing the dose burden nor requiring additional appointments for CT scanning.

Using CBCT for dosimetric evaluation necessitates image quality enhancements, which can be achieved through the correction of artefacts, occurring due to scatter detection (Siewerdsen and Jaffray 2001), detector lag and ghost (Siewerdsen and Jaffray 1999), beam hardening (Thing *et al* 2016), and scatter glare (Poludniowski *et al* 2011). Correction methods depend on a wide range of techniques such as look-up tables (Kurz *et al* 2015), Monte-Carlo calculations (Mainegra-Hing and Kawrakow 2010, Thing *et al* 2016, Zöllner *et al* 2017) or image registration (Landry *et al* 2015, Veiga *et al* 2016, Wang *et al* 2016). A deformable image registration (DIR) of the CT to the CBCT results in a virtual CT (vCT) (Peroni *et al* 2012), yielding sufficient image quality for PT dose calculation in the H&N region, but which fails for entities with more anatomical changes from fraction to fraction (Kurz *et al* 2016). To overcome those geometrical errors, the vCT along with the measured CBCT projections are used as input data for a so-called scatter correction algorithm (SCA), which in fact corrects all low frequency discrepancies such as scatter and beam hardening (Zöllner *et al* 2017). The SCA applied in this contribution, using a vCT prior, is based on works by Niu *et al* (2010), Park *et al* (2015). It results in a scatter corrected CBCT (CBCT<sub>cor</sub>) with suitable quality for proton dose calculations (Park *et al* 2015, Kurz *et al* 2016, Kim *et al* 2016, Botas *et al* 2018, Kim *et al* 2020, Andersen *et al* 2020) and has also been successfully applied for photon therapy (Hofmaier *et al* 2017). Furthermore, (Zöllner *et al* 2017) showed that the scatter estimate from the SCA approaches the expected values from a Monte Carlo simulation. Nevertheless, the feasibility of CBCT scatter correction in 4D, where new challenges, such as sparse projection data per breathing phase occur, has not yet been shown.

More recent methods for CBCT correction have been extended to tumour entities affected by intra-fractional motion in the thoracic region. Veiga *et al* (2016) showed range-corrected dose distributions on vCTs using 3D averaged images of lung cancer patients. Niepel *et al* (2019) extended the vCT approach to 4D by performing 4DCT to 4D cone beam computed tomography (4DCBCT) registration, using photon therapy CBCT scanners and iterative CBCT reconstruction by Hansen and Sørensen (2018). Bondesson *et al* (2020) applied a similar 4D approach to data from a PT CBCT scanner, using a different reconstruction approach by Mory *et al* (2016). Furthermore, in a study on simulated CBCT projections, Shrestha *et al* (2019) reconstructed a motion-compensated 4DCBCT on which carbon ion dose calculation was feasible, by deforming each phase-specific image and matching its position to that of the reference phase.

The objective of this study was to extend the 3D SCA approach to 4D by making use of our previous work on 4DvCT (Niepel *et al* 2019, Bondesson *et al* 2020), to allow time-resolved dose calculation at each PT fraction in treatment position. We extend the SCA of projections to a novel phase-based 4DCBCT correction method,



referred to as 4DCBCT<sub>cor</sub>. As a first proof of principle, the method was evaluated using a porcine lung phantom, injected with simulated lesions, with reproducible but realistic breathing motions (Biederer and Heller 2003). The phantom was used to obtain 4DCT images in two different respiratory motion patterns. One simulated a breathing pattern for planning and was used as input for 4DvCT generation, while the other was identical to the one present at the time of CBCT scanning, thus providing a ground truth for evaluation. Lesion-specific robust treatment plans, optimised on the average ground truth CT, were recalculated on all phases of both 4DCBCT<sub>cor</sub> and the ground truth 4DCT.

The accuracy of the 4DCBCT<sub>cor</sub> was evaluated by analysing images and quantitative deviations of CT numbers to the corresponding reference 4DCT. Accumulated and phase-per-phase dose distributions were compared by means of dose-volume histograms (DVHs) and gamma pass-rates (PRs). Additionally, the 4DvCT generated within the SCA workflow was compared to 4DCT in a similar fashion.

## 2. Material and methods

### 2.1. Data acquisition

Image acquisition was carried out with a 4D artiCHEST phantom (PROdesign GmbH, Germany), consisting of two hard plastic layers, the outer one filled with water, the inner one filled with an *ex vivo* porcine lung, and a water-filled diaphragm. The latter were covered with ultrasound gel to ensure motion with reduced friction. A pressure pump, which drove the diaphragm, could be manually set to realistic values for the breathing rate and amplitude (Biederer and Heller 2003). The phantom is displayed in Rabe *et al* (2021), where a more comprehensive description is outlined. Four tumours of different sizes were mimicked by injecting a gelatin-water mixture (mass concentration = 0.3 g ml<sup>-1</sup>) into the lung. The volumes of the tumours ranged from 16 to 20 cm<sup>3</sup>, being comparable in size to stage T1 or T2 NSCLC lesions (Edge and Compton 2010).

The on-board CBCT imaging system of an Elekta Synergy linac (XVI 4.5.1, Elekta, Sweden) was used for 4 min moving 4DCBCT acquisitions with a shifted detector (tube voltage = 120 kVp, tube current = 32 mA, exposure time = 20 ms, collimator = M20, filter = F1, #frames = 1320, 512 × 512 pixels, and pixel size of 0.8 mm). The exposure time and tube current were adjusted to avoid saturation and loss of object edge as described by Niepel *et al* (2019). Additionally, a Toshiba Aquilion LB (Canon Medical Systems, Japan) CT scanner was used to acquire 4DCTs with a reconstruction grid of 1.074 mm × 1.074 mm × 2 mm. The breathing signal of the 4D phantom was recorded with an Anzai belt (Anzai, Japan) and a dedicated adapter.

Changing the vacuum level in the cavity of the phantom and the pressure amplitude, used for inflating the diaphragm, provided the possibility to achieve different specific patient-like breathing curves, as the lung could be inflated and moved to a varying degree. The settings we employed generated a breathing motion of the lung with a respiration rate of 11 breaths per minute. The vacuum pump as well as the diaphragm pressure amplitude were set to obtain a large amplitude for the planning motion (plan) and a smaller one for the day-of-treatment reference motion (ref) to acquire moving images in two different configurations. A total data set containing two 4DCT scans of the moving phantom (plan and ref, respectively) with 10 phases each and one moving day-of-treatment CBCT was acquired in a single measurement session of 3.5 h. Figure 1 shows CT images of the extreme phases for both motions. Between the inhale and exhale phases the centroid positions of the injected tumours moved 2.3 mm, 3.3 mm, 5.8 mm, and 5.5 mm for the ref CT data set and 1.7 mm, 3.5 mm, 10.7 mm, and 10.8 mm for the plan CT data set, respectively.

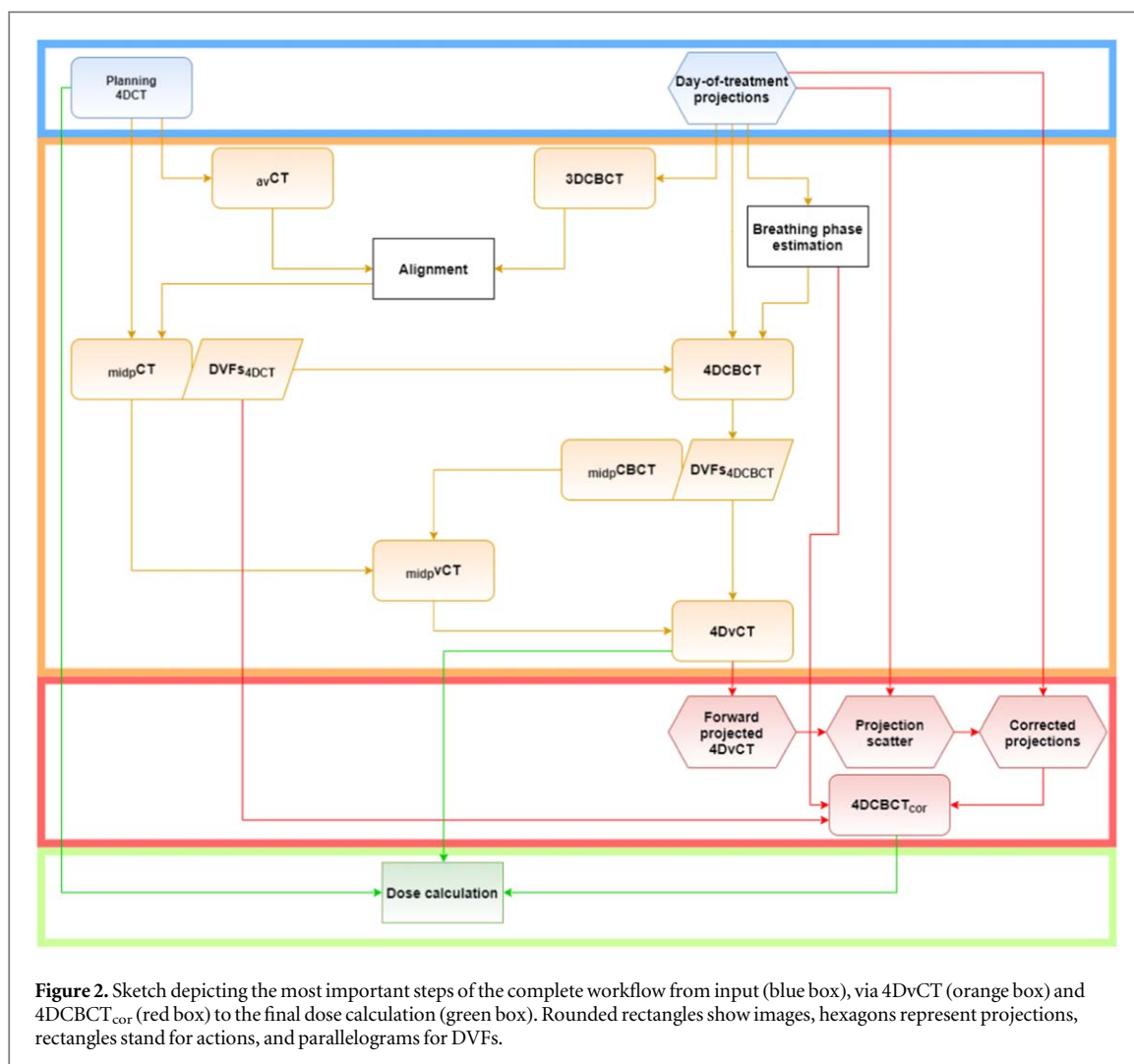


**Figure 2.** Sketch depicting the most important steps of the complete workflow from input (blue box), via 4DvCT (orange box) and 4DCBCT<sub>cor</sub> (red box) to the final dose calculation (green box). Rounded rectangles show images, hexagons represent projections, rectangles stand for actions, and parallelograms for DVFs.

## 2.2. 4DCBCT<sub>cor</sub> workflow

The workflow depicted in figure 2 was adjusted from the 4DvCT generation workflow, implemented in OpenREGGUI (<https://openreggui.org/>) and used by Bondesson *et al* (2020). 4DCT planning images and day-of-treatment 4DCBCT projections, equidistantly separated into 10 phases, were used as input for the 4DvCT workflow. Utilising a 3D Feldkamp, Davis, and Kress (FDK) algorithm (Feldkamp *et al* 1984), implemented in the reconstruction toolkit (RTK) (Rit *et al* 2014), a static average 3DCBCT image was reconstructed with  $410 \times 410 \times 264$  voxels on a  $1 \text{ mm} \times 1 \text{ mm} \times 1 \text{ mm}$  grid from the projections. Subsequently, an average CT obtained from the 10 4DCT phases was rigidly registered onto the 3DCBCT. With the help of this alignment, each of the 10 4DCT phases was transferred to the CBCT space.

### 2.2.1. Mid-positioning

A mid-position image (Wolthaus *et al* 2008a) of the 4DCT ( $\text{midpCT}$ ) was used as a starting point of this workflow because of reduced motion artefacts.

The maximum expiration phase was chosen as reference phase, since the least artefacts were expected there due to minimal motion. Deformation vector fields (DVFs) from each 4DCT phase with respect to the reference phase were determined using DIR. All DIRs were performed using a diffeomorphic Morphons algorithm (Janssens *et al* 2011) with 8 resolution scales. The number of iterations of the scales was set to 2 and 5 for the finest and second finest scales and 10 for the 6 coarsest scales. Additionally, a Gaussian regularisation of 1.25 mm standard deviation was applied. The parameters are similar to previous studies performing CT to CBCT DIR for the lung (see supplementary material of Veiga *et al* (2016) available online at [stacks.iop.org/PMB/66/175022/mmedia](https://stacks.iop.org/PMB/66/175022/mmedia)). Averaging these 10 DVFs yielded the mean motion vector field. The inverse mean motion vector field composed with each of the 10 DVFs with respect to the reference phase generated 10 DVFs with respect to the mean position. Applying this new set of DVFs ( $\text{DVF}_{s4DCT}$ ) to the corresponding 4DCT transformed each phase to the time-weighted mean position. The median of these phases yielded the motion-compensated  $\text{midpCT}$ .

### 2.2.2. 4DCBCT reconstruction

In order to extract the respiratory signal from the 4DCBCT projections, the following steps of the Amsterdam Shroud algorithm (Zijp *et al* 2004) were performed. On the original projection images, a logarithmic transform and superior-inferior derivative were conducted to enhance features in this direction, e.g. the diaphragm. Transversely summed pixels of all projections were concatenated to generate a 2D Amsterdam Shroud image, which was cropped to show only the main oscillatory signal. The phase of the analytic signal was used to determine the breathing phases. The measured CBCT projections, the breathing phases, and the 4DCT velocity fields from the mid-positioning were input data for 4DCBCT reconstruction (see the supplementary material for Amsterdam shroud image and corresponding extracted breathing phase).

The MA-ROOSTER (Mory *et al* 2016) optimisation algorithm implemented in RTK (Rit *et al* 2014) compromises between respiration-correlated techniques, showing high-contrast yet significant streaks and motion-compensated methods, which are less affected by streaks with the drawback of fully relying on a motion prior or estimate to reconstruct a single 3DCT image. MA-ROOSTER is based on ROOSTER, which uses a 4D conjugate gradient approach, that minimises the cost function  $\sum_{\alpha} \|R_{\alpha} S_{\alpha} f - p_{\alpha}\|_2^2$ , where  $R$  is a forward projection operator,  $S$  is an interpolator along the time dimension,  $f$  is a vector containing the 3D image volumes  $f_1, f_2, \dots, f_N$ ,  $N$  is the number of phases,  $p$  is the measured projection, and  $\alpha$  is the projection index. ROOSTER uses a motion mask, corresponding to a segmented region with expected movement, and therefore removing motion outside of it. Additionally, MA-ROOSTER bends the temporal regularisation to follow moving structures, so that neither small structures are smoothed away nor high-intensity structures are spread to adjacent phases.

Using the same dimension and spacing settings as for the 3DCBCT reconstruction and the DVFs<sub>4DCT</sub>, the 4DCBCT reconstruction was performed with regularisation parameters  $\gamma_{\text{space}} = 5 \cdot 10^{-4}$  and  $\gamma_{\text{time}} = 6.5 \cdot 10^{-4}$ .

$\gamma_{\text{space}}$  controlled the spatial 3D total variation for denoising the image, larger values favouring images with a lower spatial total variation (i.e. less noise). Similarly,  $\gamma_{\text{time}}$  controlled the weight given to temporal 1D total variation but after warping the images according to the DVFs which favour 4DCT images describing the same motion as the one described by the DVFs for increasing  $\gamma_{\text{time}}$ .

### 2.2.3. 4DvCT generation

The 4DCBCT mid-position image was generated analogously to the 4DCT, yielding the mid-position CBCT (<sub>midp</sub>CBCT) and DVFs<sub>4DCBCT</sub>. Subsequently, applying DIR with the same settings as described in section 2.2.1, the <sub>midp</sub>CT(plan) was registered onto the <sub>midp</sub>CBCT(day-of-treatment) yielding a mid-position vCT (<sub>midp</sub>vCT). The inverted DVFs<sub>4DCBCT</sub> were applied subsequently onto the <sub>midp</sub>vCT to obtain a 4DvCT. This workflow was previously presented and evaluated in Bondesson *et al* (2020).

## 2.3. Scatter correction

The SCA was based on works by Park *et al* (2015) and Niu *et al* (2010). It was conducted on a per-phase level, meaning that the inputs were a single phase of the 4DvCT and the corresponding 4DCBCT projections

$$p_{\text{raw},\alpha} = -\ln \frac{I_{\text{raw},\alpha}}{I_0}, \quad (1)$$

where  $I_{\text{raw},\alpha}$  is the total intensity measured by the CBCT detector and  $I_0$  is the open field intensity. The raw intensity ( $I_{\text{raw},\alpha}$ ) consists of a scatter component ( $I_{\text{sca},\alpha}$ ) and a primary component ( $I_{\text{pri},\alpha}$ ). The latter was calculated by applying the forward projection operator  $R$  to the vCT phase according to the CBCT geometry using RTK and was assumed to be scatter-free. Accounting for the tube current-exposure time (mA s) per projection, a correction factor of 4.0, defined as the ratio of a reference value mAs (tube current = 64 mA, exposure time = 40 ms) and the measured CBCT acquisition mAs (32 mA, 20 ms), was multiplied with  $I_{\text{raw},\alpha}$ . Subtracting these projections from each other and convolving them with a generous smoothing filter ( $F$ ), as described in Kurz *et al* (2016), led to projection scatter ( $I_{\text{sca},\alpha}$ )

$$I_{\text{sca},\alpha} = F(I_{\text{raw},\alpha} \cdot \text{CF} - I_{\text{pri},\alpha}). \quad (2)$$

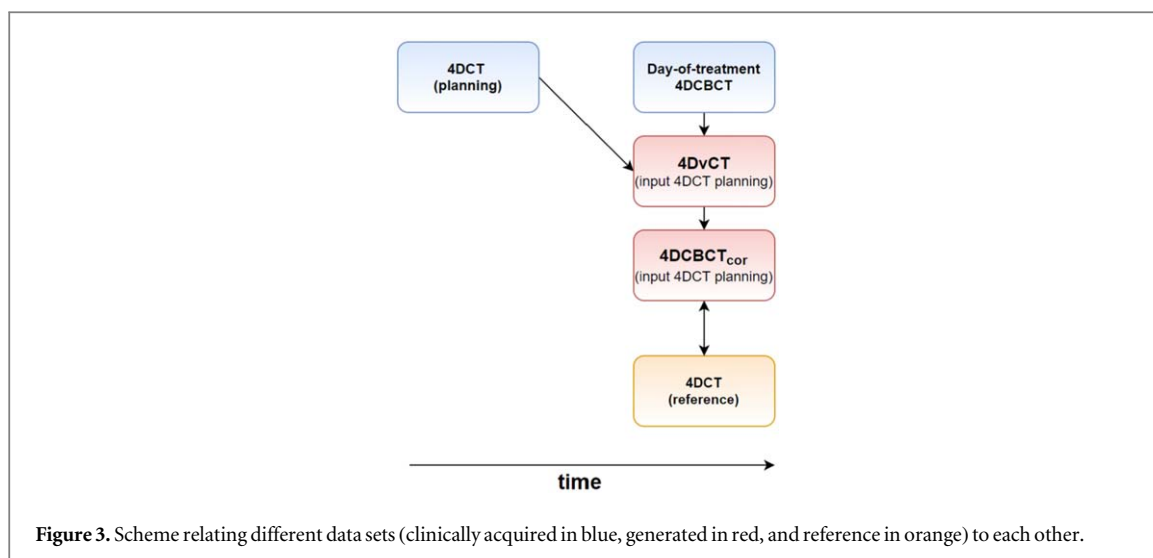
Subtracting  $I_{\text{sca},\alpha}$  from the measured  $I_{\text{raw},\alpha}$  generated corrected projections ( $I_{\text{cor},\alpha}$ )

$$I_{\text{cor},\alpha} = I_{\text{raw},\alpha} \cdot \text{CF} - I_{\text{sca},\alpha}. \quad (3)$$

Applying this successively to all of the 10 phases, a set of corrected projections was obtained. Utilising MA-ROOSTER, the log-transformed corrected projections ( $p_{\text{cor},\alpha} = -\ln I_{\text{cor},\alpha}/I_0$ ) were reconstructed to the 4DCBCT<sub>cor</sub>, analogously to the 4DCBCT, with the same vector fields and settings.

## 2.4. Treatment planning

The day-of-treatment 4DCT dataset was aligned to the CBCT space as described in section 2.2. All ten phases of the day-of-treatment 4DCT, 4DvCT, and 4DCBCT<sub>cor</sub>, using the same generic CT density calibration curve, were transferred to the research version 8.99 of the commercial treatment planning system RayStation (RaySearch



Laboratories, Sweden), on which treatment was planned. We used a beam model corresponding to a generic IBA pencil beam scanning beamline and nozzle ('RSL\_IBA\_DED'). The four different simulated tumours were contoured on all 4DCT phases. For all lesions, internal target volumes (ITVs) were created, which were then copied to the average CT. A density override of each ITV was performed using muscle tissue with a density of  $1.05 \text{ g cm}^{-3}$  (Meijers *et al* 2020a, Ribeiro *et al* 2021).

For each of the four ITVs, a 3D robust optimised pencil beam scanning proton treatment plan administering 60 Gy in 30 fractions with a 3-field arrangement was created on the average CT. The field angles were set to avoid sharp edges and screws of the phantom. The beams were optimised simultaneously. The specific angles are stated in the supplementary material. The Monte Carlo dose engine was used during plan optimisation with a statistical error of 1%. Following (Meijers *et al* 2020a), the clinical robustness settings (range error =  $\pm 3\%$ , setup error =  $\pm 6 \text{ mm}$ ) were used. The robust optimisation used a minmax method, in which the worst-case scenario regarding the optimisation functions is considered (Fredriksson *et al* 2011). Each IMPT plan fulfilled the clinical goal of at least 95% volume above 57 Gy and was optimised using a constant relative biological effectiveness of 1.1 (Paganetti *et al* 2002). Subsequently, all four plans were re-computed on every phase and modality (day-of-treatment 4DCT, 4DvCT, 4DCBCT<sub>cor</sub>) without density override, generating a total of 120 different dose distributions.

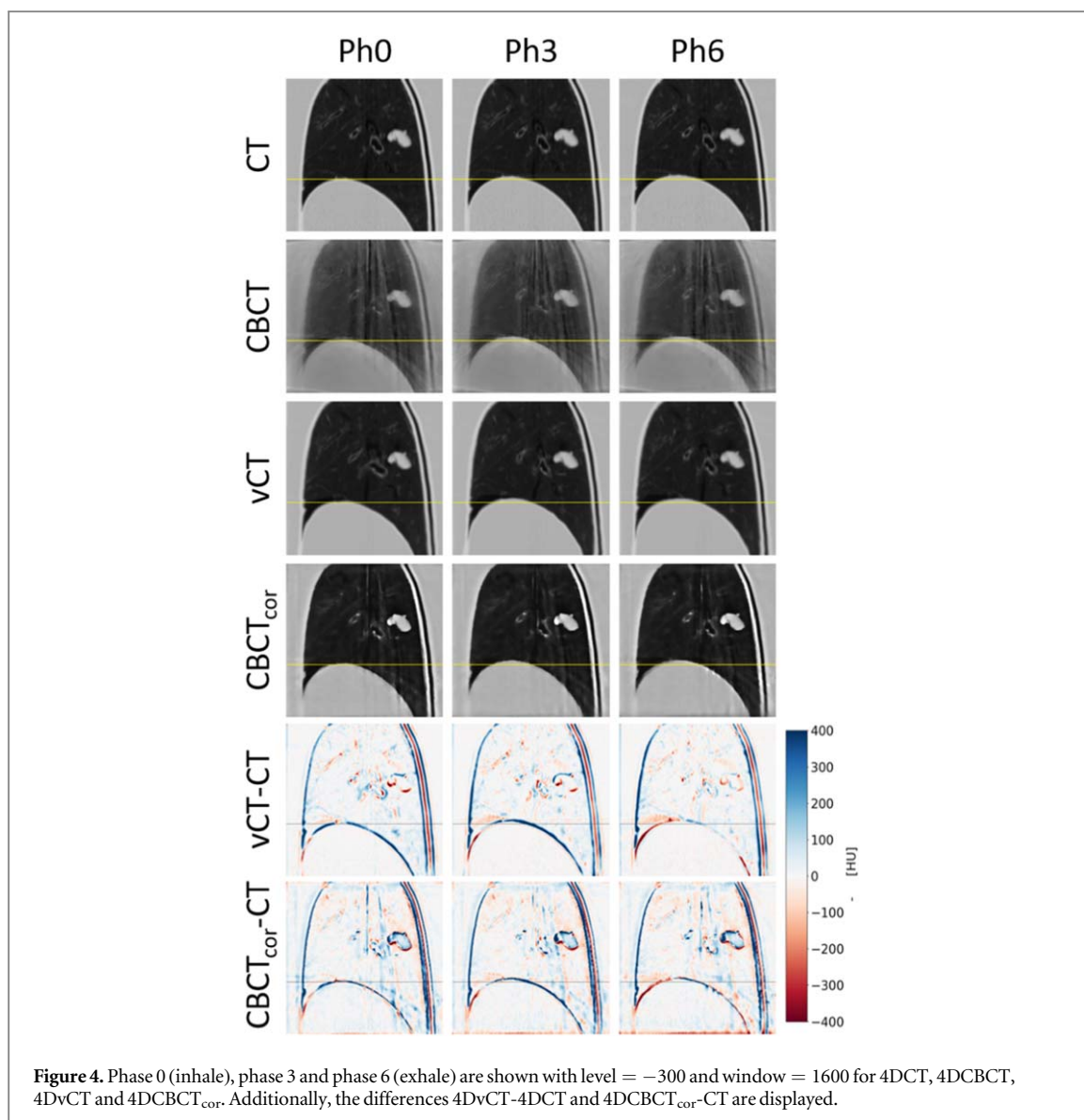
## 2.5. Computer hardware

DIR, reconstruction, and filtering were performed on a computer with two Intel Xeon E5-2630 v3 processors at 2.4 GHz with each having 8 physical cores and hyper-threading enabled, resulting in a total of 32 threads. The GPU was a Nvidia Quadro P6000 with 24 GB memory.

## 2.6. Data analysis

Figure 3 shows an overview relating the different data sets to each other. The blue coloured boxes represent the data sets, which would be typically acquired in a clinical setting. The red background colour represents the image sets, which were generated as explained in section 2.2. In order to assess the accuracy of these generated images an additional 4DCT, shown in orange, was acquired with the same day-of-treatment breathing motion as the 4DCBCT, which was different to the motion of the initial planning 4DCT.

The image quality of the different 4D modalities was analysed using difference plots and mean error (ME) calculations in terms of CT numbers in Hounsfield unit (HU) with the day-of-treatment 4DCT as reference. The 4DvCT and 4DCBCT<sub>cor</sub> methods were further evaluated by comparing DVH parameters ( $D_{2\%}$ ,  $D_{98\%}$ ,  $D_{\text{mean,ITV}}$ ,  $D_{\text{mean,lung}}$ ) and calculating global gamma PR using (3%, 3 mm) and (2%, 2 mm) criteria with a 10% dose threshold for lesion-specific robust proton plans versus day-of-treatment reference 4DCT for individual phases and accumulated doses. Accumulated doses were calculated for each 4D image and ITV of each lesion. The accumulation was done by applying the DVFs<sub>4DCT</sub> to the respective 4DCT phase doses and the DVFs<sub>4DCBCT</sub> to the respective phase doses of 4DvCT and 4DCBCT<sub>cor</sub> and averaging the results.



### 3. Results

#### 3.1. Comparison between different modalities

Figure 4 displays an exemplary sagittal slice of 4DCT(ref), 4DCBCT, 4DvCT and 4DCBCT<sub>cor</sub> for phases 0 (inhale), 3 and 6 (exhale) as well as corresponding image differences. Quality enhancements in 4DvCT and 4DCBCT<sub>cor</sub> compared to 4DCBCT were observed. The 4DvCT showed the expected low-noise images similar to the 4DCT. Both the 4DvCT and 4DCBCT<sub>cor</sub> showed good agreement to the 4DCT in regions of homogeneous tissue. At boundaries, such as the diaphragm-lung interface, differences of more than 100 HU were observed.

##### 3.1.1. Line profiles

Figure 5 shows two line profiles for all modalities for the inhale and exhale phases in the inferior–superior direction as indicated with the yellow arrows on the thumbnails on top of each plot. Both plots show similar behaviour in CT numbers for CT, vCT, and CBCT<sub>cor</sub>. The original CBCT with non-corrected HU systematically underestimated the diaphragm (left side of the plots), tumour (centre of the plots), and shell (right side of the plots) values by around 200 HU to the reference CT, while it overestimated the values in lung tissue by roughly the same amount. At the edges of the diaphragm and the outer shell, as well as inside the tumour, CBCT<sub>cor</sub> consistently overestimated HU values compared to CT and vCT.

##### 3.1.2. Mean error

Figure 6 shows three different ME plots in HU versus phase for the three contours lung, body (whole phantom), and outer shell. Each sub-figure compares the reference CT with one of the three remaining images. The top



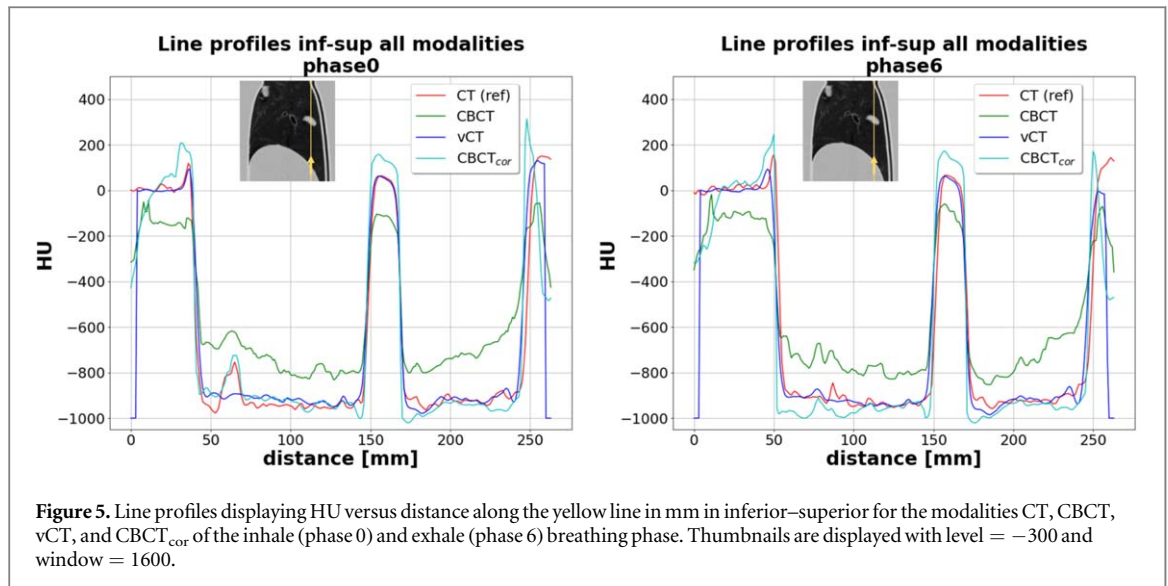


Figure 5. Line profiles displaying HU versus distance along the yellow line in mm in inferior–superior for the modalities CT, CBCT, vCT, and CBCT<sub>cor</sub> of the inhale (phase 0) and exhale (phase 6) breathing phase. Thumbnails are displayed with level = -300 and window = 1600.

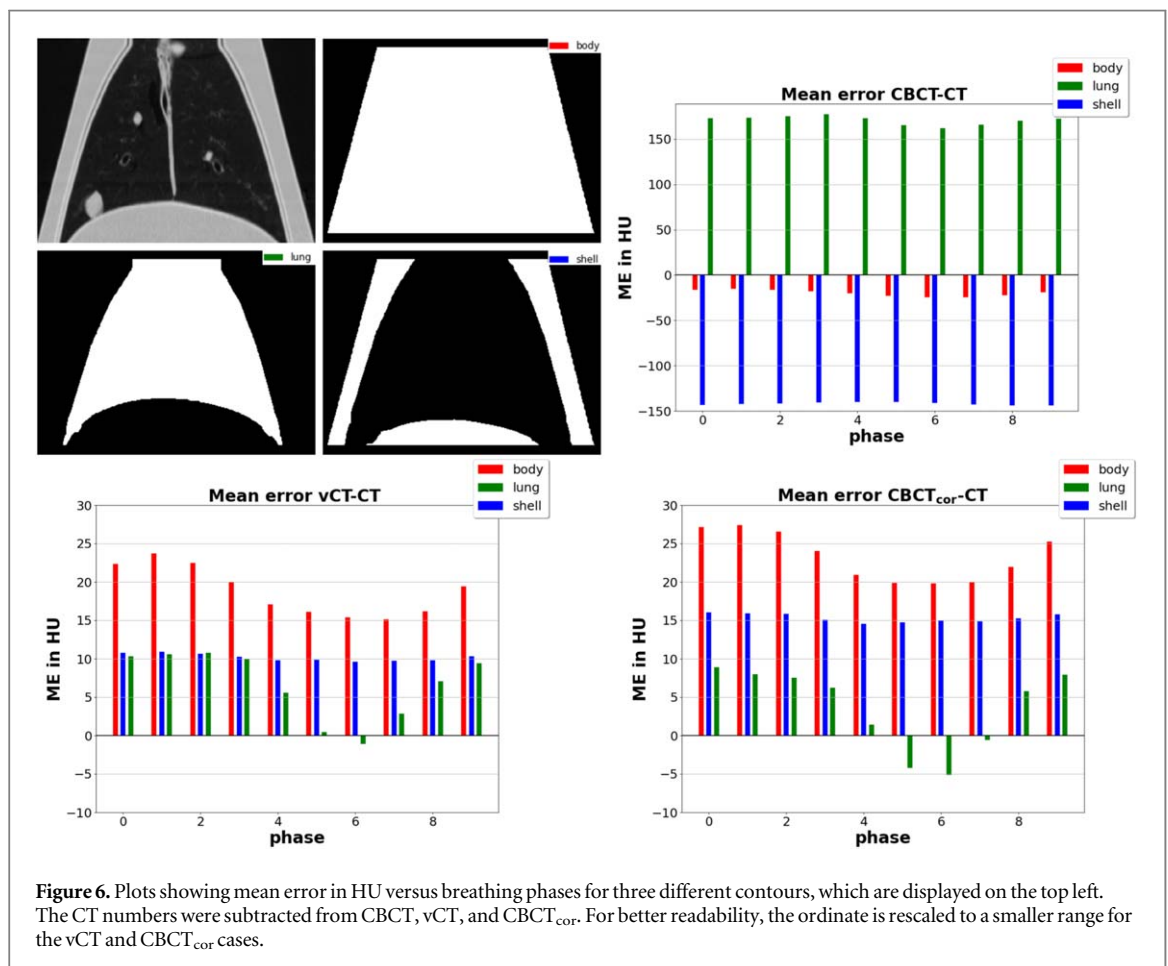
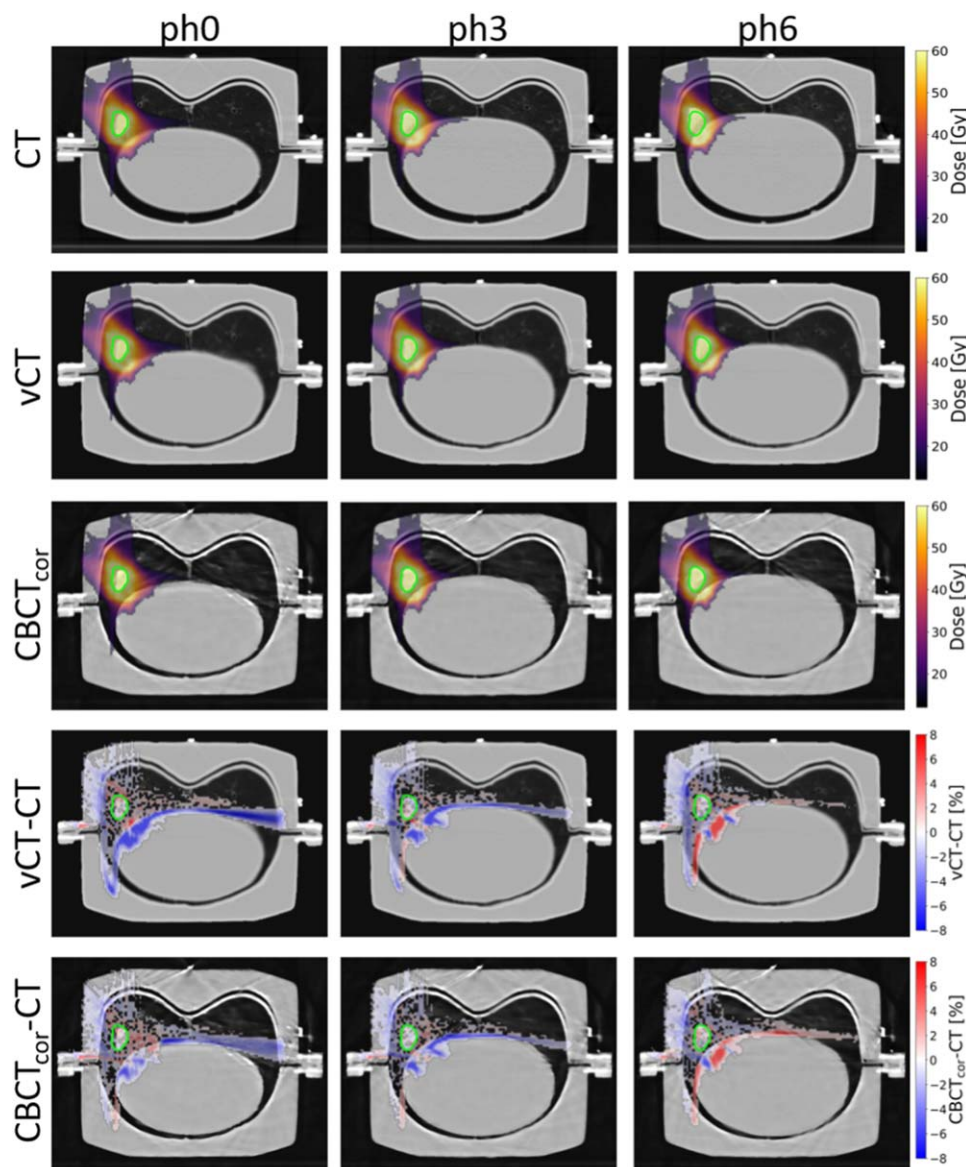


Figure 6. Plots showing mean error in HU versus breathing phases for three different contours, which are displayed on the top left. The CT numbers were subtracted from CBCT, vCT, and CBCT<sub>cor</sub>. For better readability, the ordinate is rescaled to a smaller range for the vCT and CBCT<sub>cor</sub> cases.

right sub-figure, comparing CT and original CBCT, shows substantial discrepancies as expected. The two bottom sub-figures showed similar results with reduced deviations. The ME differences for the lung contour, which varied in absolute terms between close to 0 and slightly above (vCT) or below (CBCT<sub>cor</sub>) 10 HU, changed sign for phases close to the exhale phase 6. Consequently, the body contour, which was the union of lung and shell, showed reduced errors close to the maximum breathing amplitude. The values of the shell remained approximately constant throughout all different phases with difference values of around 10 HU (vCT) and 15 HU (CBCT<sub>cor</sub>), respectively.



**Figure 7.** Proton dose distributions of ITV<sub>4</sub> are displayed. To improve clarity, no values below 15 Gy are shown in the CT, vCT, and CBCT<sub>cor</sub> cases. For better readability, of the difference plots vCT and CBCT<sub>cor</sub> to the CT (expressed as a percentage of the prescribed dose), absolute dose differences smaller than 0.4% are masked. The CTs are shown with level = −300 and window = 1600 for phase 0 (inhale), phase 3, and phase 6 (exhale).

### 3.2. Proton dose analysis

Figure 7 displays axial slices of proton dose distributions of the ITV<sub>4</sub> plan, calculated on phases 0, 3, and 6 of CT, vCT, and CBCT<sub>cor</sub>. Additionally, dose difference plots between vCT and CBCT<sub>cor</sub> to CT are shown. A good agreement was observed for vCT and CBCT<sub>cor</sub>. Only minor deviations of a few percent between reference CT images and generated vCT and CBCT<sub>cor</sub> and within different phases were found.

#### 3.2.1. Dose-volume histograms

DVHs for exemplary ITV<sub>4</sub> and the lung are presented in figure 8 for inhale and exhale phase and the accumulated dose. The images confirm good agreement in all scenarios. On the right tail of the DVH curve of ITV<sub>4</sub>, slightly larger dose values for vCT and CBCT<sub>cor</sub> were seen on both extreme phases. Overall smaller deviations were detected for the lung. For ITV<sub>4</sub>, the vCT-CT difference  $\Delta D_{2\%}$ ,  $\Delta D_{98\%}$  are for phase 0 −1.0%, −1.0%, for phase 6 0.1%, −0.5% and for the accumulated dose 0.2%, 0.1%. The corresponding values for the CBCT<sub>cor</sub>-CT difference are for phase 0 −0.7%, −0.5%, for phase 6 −0.2%, −0.7% and for the accumulated dose 0.0%, 0.8%.

Table 1 displays differences in DVH parameters for accumulated dose calculations on vCT and CBCT<sub>cor</sub> to the corresponding CT. The values confirmed the good agreement as  $\Delta D_{2\%}$  and  $\Delta D_{98\%}$  were not larger than 2%

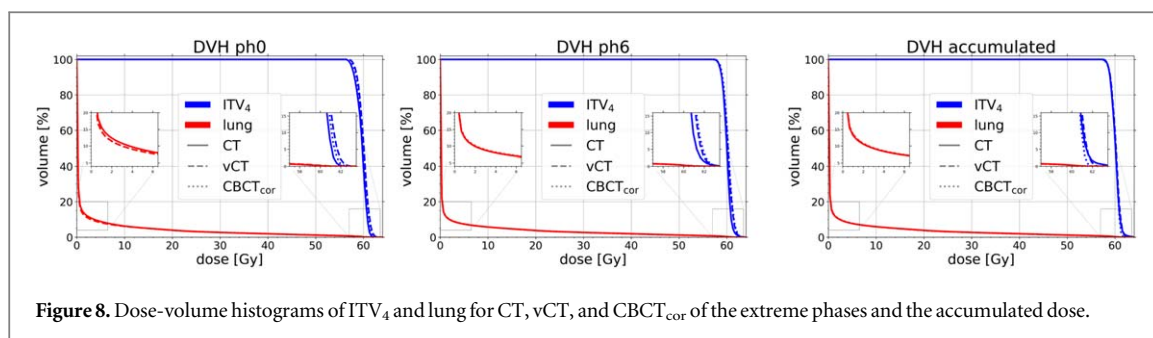


Figure 8. Dose-volume histograms of ITV<sub>4</sub> and lung for CT, vCT, and CBCT<sub>cor</sub> of the extreme phases and the accumulated dose.

Table 1. Relative differences between accumulated dose on vCT and CBCT<sub>cor</sub> to CT in  $D_{2\%}$ ,  $D_{98\%}$ ,  $D_{mean,ITV}$  and  $D_{mean,lung}$  for all plans. All dose difference values are displayed in percent.

| vCT                   |                  | CBCT <sub>cor</sub> |                  | vCT                    |                  | CBCT <sub>cor</sub> |                  |
|-----------------------|------------------|---------------------|------------------|------------------------|------------------|---------------------|------------------|
| ITV <sub>1</sub>      | ITV <sub>2</sub> | ITV <sub>1</sub>    | ITV <sub>2</sub> | ITV <sub>1</sub>       | ITV <sub>2</sub> | ITV <sub>1</sub>    | ITV <sub>2</sub> |
| ITV <sub>3</sub>      | ITV <sub>4</sub> | ITV <sub>3</sub>    | ITV <sub>4</sub> | ITV <sub>3</sub>       | ITV <sub>4</sub> | ITV <sub>3</sub>    | ITV <sub>4</sub> |
| $\Delta D_{2\%}$      |                  |                     |                  | $\Delta D_{98\%}$      |                  |                     |                  |
| 1.7%                  | -0.1%            | 2.0%                | -0.2%            | 1.3%                   | 1.2%             | 1.6%                | 1.4%             |
| 0.4%                  | 0.2%             | -0.1%               | 0.0%             | 0.8%                   | 0.1%             | 0.9%                | 0.8%             |
| $\Delta D_{mean,ITV}$ |                  |                     |                  | $\Delta D_{mean,lung}$ |                  |                     |                  |
| 0.9%                  | 0.4%             | 1.0%                | 0.4%             | 1.1%                   | 1.3%             | 1.0%                | 1.2%             |
| 0.3%                  | -0.1%            | 0.4%                | 0.0%             | -1.2%                  | 1.0%             | -0.5%               | 0.6%             |

Table 2. Gamma-index PR in percent for two different global criteria with a fixed dose threshold of 10%. The accumulated doses of vCT and CBCT<sub>cor</sub> were compared to the corresponding dose values on CT.

| Plan             | vCT        | CBCT <sub>cor</sub> | vCT        | CBCT <sub>cor</sub> |
|------------------|------------|---------------------|------------|---------------------|
|                  | (3%, 3 mm) |                     | (2%, 2 mm) |                     |
| ITV <sub>1</sub> | 97.3       | 98.3                | 93.4       | 94.2                |
| ITV <sub>2</sub> | 98.7       | 99.3                | 93.2       | 95.5                |
| ITV <sub>3</sub> | 97.6       | 98.4                | 94.7       | 95.7                |
| ITV <sub>4</sub> | 99.7       | 99.7                | 97.5       | 97.9                |

for all vCT and CBCT<sub>cor</sub> comparisons with respect to the CT. Mean dose values for ITV and lung had a maximum deviation of 1.3% over all cases.

Quantitative results regarding the proton dose comparison are summarised in table 2, displaying gamma PR for accumulated doses of vCT and CBCT<sub>cor</sub> compared to CT for two gamma criteria and all four plans. The gamma PR for vCT and CBCT<sub>cor</sub> were between 97% and 100% for a (3%, 3 mm) criterion and between 93% and 98% for a (2%, 2 mm) criterion. DVH parameters and gamma PR results on a per-phase level are shown in the supplementary material.

#### 4. Discussion

A novel algorithm for 4DCBCT correction, which is based on 4DvCT, was successfully implemented and evaluated. The acquisition of CT and CBCT scans of the porcine lung phantom, with a reproducible breathing motion in a geometry similar to the human thorax, allowed for a 4DCT ground truth image and thus the experimental evaluation of the 4DCBCT<sub>cor</sub> method and comparison to the intermediate 4DvCT step. Proton dose calculation was feasible and accurate on both 4DvCT and 4DCBCT<sub>cor</sub> for the porcine lung phantom scans. The 4DCBCT<sub>cor</sub> was evaluated in the context of PT for the first time. Accumulated doses calculated on the 4DvCT and 4DCBCT<sub>cor</sub> were in good agreement with those calculated on the reference 4DCT. DVH parameter comparisons deviated at most 1.7% in the 4DvCT and 2.0% in the 4DCBCT<sub>cor</sub> case, respectively. Additionally, gamma PR for a (3%, 3 mm) criterion with 10% threshold were at least 97.3% (4DvCT) and 98.3% (4DCBCT<sub>cor</sub>). The motion amplitude between inhale and exhale for the centroid positions of the simulated tumours ranged from 2.3 to 10.8 mm, which is in accordance to the range typically observed in clinical routine

(Wolthaus *et al* 2008b). The observed dose calculation accuracy was very similar between the four different simulated tumours, which were distributed in the lung and had different extents of motion.

Measuring doses would be of interest but remains challenging due to the closed shell of the porcine phantom. A study by Mann *et al* (2016) investigated the same porcine phantom in combination with a dosimetric gel. This MRI study reported a high agreement between measured and calculated doses while achieving a homogeneous coverage of the PTV. The measurements showed a gamma PR between 87.4% and 94.4% for a (3%, 3 mm) criterion.

A range analysis was not conducted since small differences become extensive in lung tissue, due to its low density. The DVH and gamma analysis results are comparable to those reported by Shrestha *et al* (2019) for a 4DCBCT carbon-ion lung cancer study, which used simulated projections and a motion-compensated reconstruction algorithm. Furthermore, the DVH analysis and gamma PR showed good agreement to previous 4DvCT studies. Niepel *et al* (2019) used a different reconstruction (Hansen and Sørensen 2018) and vCT generation approach which relied on phase-per-phase CT to CBCT Morphons DIR; they obtained phase-specific (3%, 3 mm) PR above 95% for a two-field plan and did not consider accumulated doses. Bondesson *et al* (2020) applied the 4DvCT algorithm used in this work to a PT-specific CBCT scanner and obtained accumulated dose (3%, 3 mm) PR > 95%. Both studies did not use injected simulated tumours but used residual tissues as surrogates.

It should be noted that, in our study, DVH difference values were in most cases slightly larger for the 4DCBCT<sub>cor</sub> than the 4DvCT, whereas for the gamma PR slightly larger values were achieved with the 4DCBCT<sub>cor</sub>. These minor differences of a few tenths of a percent can likely be explained by the difference in regions of interest. DVHs relate to voxels inside specific organs, while the gamma evaluation covers the dose volume covered by the 10% isodose.

For 4DCBCT<sub>cor</sub>, it should be stressed that large anatomical changes, which DIR cannot always model accurately, could not be simulated in our experimental setup. Consequently, we could not demonstrate the better anatomical fidelity for CBCT<sub>cor</sub> over vCT reported by Kurz *et al* (2016), who analysed the difference of 3DCBCT<sub>cor</sub> and 3DvCT by comparing the contours of PTV, CTV, bladder, and rectum to reference contours made on the initial 3DCBCT. The 3DCBCT<sub>cor</sub>-based contours showed an improved agreement with the reference 3DCBCT contours over the 3DvCT ones, which were hampered by inaccurate DIR.

Since tumour shrinkage and pleural effusion might be difficult to model by DIR, it is likely that 4DCBCT<sub>cor</sub> is beneficial in such scenarios. Cavity correction steps, which address these limitations of DIR, have been proposed by Veiga *et al* (2016) and would be needed for 4DCBCT<sub>cor</sub>.

Similar visual improvements were observed in studies of static targets (Park *et al* 2015, Kurz *et al* 2016) in 3D, although one should keep in mind that these studies relied on FDK reconstructions. Additionally, the reported gamma PR of these patient studies were in the same order of magnitude as in our study. Kurz *et al* (2016) values are not directly comparable as different regions were investigated. However, Park *et al* (2015) reports for lung 98.6% (3%, 3 mm) and 93.0% (2%, 2 mm), which is similar to our values.

The constant overshoot of CT numbers in the 4DCBCT images might originate from differences in the x-ray spectra, beam hardening, and spectral response of the CT and CBCT, which might not be perfectly captured by our scatter correction approach. Overshoot observed at the edges of the tumour and the shell, might also be caused by the DIR and the resampling steps, leading to a slight blurring of the vCT images used for generating CBCT<sub>cor</sub>. However, the different impact of these effects cannot be resolved within our experimental set-up and thus remains unknown.

By applying different breathing motions for the planning and reference states, we could show that the DIR can be employed successfully, yielding good geometric agreement between the 4DvCT and reference 4DCT images. Minor, yet perceptible, misalignments of diaphragm and shell were visible in our study. These residual mismatches led to divergences at boundaries such as the diaphragm-lung interface (see figure 4). Nevertheless, the feasibility of deforming a 4DCT into a 4DvCT with updated motion, which can be used as a prior for scatter correction eventually yielding the 4DCBCT<sub>cor</sub>, can be concluded.

As stated above, the porcine lung phantom, having a constant breathing pattern and non-varying anatomy, is an ideal tool for proof-of-principle studies, as demonstrated in various applications such as MR motion tracking (Rabe *et al* 2021) or proton radiography-based range uncertainty assessment (Meijers *et al* 2020b). However, the workflow has to be evaluated with clinical data of lung patients in a next step. Lung cases with changing tumour sizes over the course of the treatment, which as stated above could not be simulated in this study, would be of particular interest.

However, studies with patient data usually lack ground truth information as the same reproducible breathing motion and patient setup between the different acquisitions cannot be provided. The phantom allows to comprehensively evaluate the method before applying it to patient cases. This stresses the value of first performing proof-of-principle phantom studies (Landry *et al* 2014).

When applied to patient data, the 4DCBCT<sub>cor</sub> method would allow dose reconstruction by splitting the dose plan into different phases similar to Ribeiro *et al* (2021). This offers the advantage to account for the interplay between respiratory motion and pencil beam delivery in the geometry of the patient setup right before treatment and may permit protocol robustness evaluation without the need of additional 4DCT scans. Furthermore, this method would have the potential to be used for daily online dose adaptation in the future.

Before application in clinical online scenarios, the needed computation time would have to be addressed. In this proof-of-concept study, no special effort was made to accelerate the computation, resulting in runtimes of roughly 4 h for the entire workflow. The 4DvCT workflow, as a prerequisite of the 4DCBCT<sub>cor</sub> workflow, currently takes roughly 3.5 h. The successive 4DCBCT<sub>cor</sub> workflow, whose runtime again is not optimised, currently needs around 30 min. Current bottlenecks are DIRs using a Morphons algorithm, 4DCBCT and 4DCBCT<sub>cor</sub> reconstructions using MA-ROOSTER, and filtering during the scatter correction, which needs to be conducted separately for each phase. Further overall parallelisation and GPU-based filtering could speed up the process. Another promising approach would be to use deep learning also in 4D since it was successfully applied to 3DCBCT correction scenarios in the last years (Hansen *et al* 2018, Kurz *et al* 2019, Landry *et al* 2019, Thummerer *et al* 2020, Chen *et al* 2020a).

## 5. Conclusions

In this work, a 4DCBCT<sub>cor</sub> technique, based on a phase-per-phase scatter correction, which uses a 4DvCT as a prior, has been investigated for proton dose calculations on porcine lung phantom data. The results of this experimental validation study for 4DCBCT<sub>cor</sub> showed usability for accurate proton dose calculation. A similar performance was observed for the 4DvCT. The applied method generates up-to-date in-room images, accounting for breathing motion and potentially anatomical changes, and is thus of clinical interest for daily 4D proton dose estimation.

## Acknowledgments

Katharina Niepel, Jan Hofmaier, and Vanessa Filipa da Silva Mendes are thanked for support related to CBCT projection acquisition. This work was supported by the German Research Foundation (DFG) project number 399 148 265 and Research Training Group GRK 2274, as well as by the FöFoLe commission of the Medical Faculty of the LMU Munich under grant 1056.

## ORCID iDs

Henning Schmitz  <https://orcid.org/0000-0001-6143-1187>

Moritz Rabe  <https://orcid.org/0000-0002-7085-4066>

Guillaume Janssens  <https://orcid.org/0000-0001-9553-6024>

David Bondesson  <https://orcid.org/0000-0003-3112-886X>

Katia Parodi  <https://orcid.org/0000-0001-7779-6690>

Guillaume Landry  <https://orcid.org/0000-0003-1707-4068>

## References

- Albertini F, Matter M, Nenoff L, Zhang Y and Lomax A 2020 Online daily adaptive proton therapy *Br. J. Radiol.* **93** 110720190594
- Andersen A G, Park Y-K, Elström U V, Petersen J B B, Sharp G C, Winey B, Dong L and Muren L P 2020 Evaluation of an a priori scatter correction algorithm for cone-beam computed tomography based range and dose calculations in proton therapy *Phys. Imaging Radiat. Oncol.* **16** 89–94
- Berman A, James S and Rengan R 2015 Proton beam therapy for non-small cell lung cancer: current clinical evidence and future directions *Cancers* **7** 1178–90
- Biederer J and Heller M 2003 Artificial thorax for MR imaging studies in porcine heart-lung preparations *Radiology* **226** 250–5
- Bondesson *et al* 2020 Anthropomorphic lung phantom based validation of in-room proton therapy 4D-CBCT image correction for dose calculation *Z. Med. Phys.* (<https://doi.org/10.1016/j.zemedi.2020.09.004>)
- Botas P, Kim J, Winey B and Paganetti H 2018 Online adaption approaches for intensity modulated proton therapy for head and neck patients based on cone beam CTs and Monte Carlo simulations *Phys. Med. Biol.* **64** 015004
- Chen L, Liang X, Shen C, Jiang S and Wang J 2020a Synthetic CT generation from CBCT images via deep learning *Med. Phys.* **47** 1115–25
- Chen M, Yang J, Liao Z, Chen J, Xu C, He X, Zhang X, Zhu R X and Li H 2020b Anatomic change over the course of treatment for non-small cell lung cancer patients and its impact on intensity-modulated radiation therapy and passive-scattering proton therapy deliveries *Radiat. Oncol.* **15** 55
- Edge S B and Compton C C 2010 The American joint committee on cancer: the VII edition of the AJCC cancer staging manual and the future of TNM *Ann. Surg. Oncol.* **17** 1471–4
- Feldkamp L A, Davis L C and Kress J W 1984 Practical cone-beam algorithm *J. Opt. Soc. Am. A* **1** 612–9

- Fredriksson A, Forsgren A and Hårdemark B 2011 Minimax optimization for handling range and setup uncertainties in proton therapy *Med. Phys.* **38** 1672–84
- Hansen D C, Landry G, Kamp F, Li M, Belka C, Parodi K and Kurz C 2018 ScatterNet: A convolutional neural network for cone-beam CT intensity correction *Med. Phys.* **45** 4916–26
- Hansen D C and Sørensen T S 2018 Fast 4D cone-beam CT from 60s acquisitions *Phys. Imaging Radiat. Oncol.* **5** 69–75
- Hoffmann L, Alber M, Jensen M F, Holt M I and Møller D S 2017 Adaptation is mandatory for intensity modulated proton therapy of advanced lung cancer to ensure target coverage *Radiother. Oncol.* **122** 400–405
- Hofmaier J et al 2017 Multi-criterial patient positioning based on dose recalculation on scatter-corrected CBCT images *Radiother. Oncol.* **125** 464–9
- Jakobi A, Perrin R, Knopf A and Richter C 2017 Feasibility of proton pencil beam scanning treatment of free-breathing lung cancer patients *Acta Oncol.* **57** 203–10
- Janssens G, Jacques L, de Xivry J O, Geets X and Macq B 2011 Diffeomorphic registration of images with variable contrast enhancement *Int. J. Biomed. Imaging* **2011** 1–16
- Keall P et al 2006 The management of respiratory motion in radiation oncology report of AAPM task group 76a) *Med. Phys.* **33** 3874–900
- Kim H, Pyo H, Noh J M, Lee W, Park B, Park H Y and Yoo H 2019 Preliminary result of definitive radiotherapy in patients with non-small cell lung cancer who have underlying idiopathic pulmonary fibrosis: comparison between x-ray and proton therapy *Radiat. Oncol.* **14** 19
- Kim J, Park Y-K, Sharp G, Busse P and Winey B 2016 Water equivalent path length calculations using scatter-corrected head and neck CBCT images to evaluate patients for adaptive proton therapy *Phys. Med. Biol.* **62** 59–72
- Kim J, Park Y-K, Sharp G, Busse P and Winey B 2020 Beam angle optimization using angular dependency of range variation assessed via water equivalent path length (WEPL) calculation for head and neck proton therapy *Phys. Med.* **69** 19–27
- Kurz C, Dedes G, Resch A, Reiner M, Ganswindt U, Nijhuis R, Thieke C, Belka C, Parodi K and Landry G 2015 Comparing cone-beam CT intensity correction methods for dose recalculation in adaptive intensity-modulated photon and proton therapy for head and neck cancer *Acta Oncol.* **54** 1651–7
- Kurz C, Maspero M, Savenije M H F, Landry G, Kamp F, Pinto M, Li M, Parodi K, Belka C and van den Berg C A T 2019 CBCT correction using a cycle-consistent generative adversarial network and unpaired training to enable photon and proton dose calculation *Phys. Med. Biol.* **64** 22225004
- Kurz C et al 2016 Investigating deformable image registration and scatter correction for CBCT-based dose calculation in adaptive IMPT *Med. Phys.* **43** 5635–46
- Lalonde A, Winey B, Verburg J, Paganetti H and Sharp G C 2020 Evaluation of CBCT scatter correction using deep convolutional neural networks for head and neck adaptive proton therapy *Phys. Med. Biol.* **65** 24245022
- Landry G, Hansen D, Kamp F, Li M, Hoyle B, Weller J, Parodi K, Belka C and Kurz C 2019 Comparing Unet training with three different datasets to correct CBCT images for prostate radiotherapy dose calculations *Phys. Med. Biol.* **64** 3035011
- Landry G and Hua C 2018 Current state and future applications of radiological image guidance for particle therapy *Med. Phys.* **45** 11
- Landry G et al 2014 Phantom based evaluation of CT to CBCT image registration for proton therapy dose recalculation *Phys. Med. Biol.* **60** 595–613
- Landry G et al 2015 Investigating CT to CBCT image registration for head and neck proton therapy as a tool for daily dose recalculation *Med. Phys.* **42** 1354–66
- Lin M et al 2020 Radiation therapy for pediatric brain tumors using robotic radiation delivery system and intensity modulated proton therapy *Pract. Radiat. Oncol.* **10** e173–82
- Lomax A J, Pedroni E, Rutz H P and Goitein G 2004 The clinical potential of intensity modulated proton therapy *Z. Med. Phys.* **14** 147–52
- Lomax A et al 2001 Intensity modulated proton therapy: a clinical example *Med. Phys.* **28** 317–24
- Mainegra-Hing E and Kawrakow I 2010 Variance reduction techniques for fast monte carlo CBCT scatter correction calculations *Phys. Med. Biol.* **55** 4495–507
- Mann P, Witte M, Moser T, Lang C, Runz A, Johnen W, Berger M, Biederer J and Karger C P 2016 3d dosimetric validation of motion compensation concepts in radiotherapy using an anthropomorphic dynamic lung phantom *Phys. Med. Biol.* **62** 573–95
- Manzar G et al 2020 Comparative analysis of acute toxicities and patient reported outcomes between intensity-modulated proton therapy (IMPT) and volumetric modulated arc therapy (VMAT) for the treatment of oropharyngeal cancer *Radiother. Oncol.* **147** 64–74
- McClelland J R, Hughes S, Modat M, Qureshi A, Ahmad S, Landau D B, Ourselin S and Hawkes D J 2010 Inter-fraction variations in respiratory motion models *Phys. Med. Biol.* **56** 251–72
- Meijers A, Knopf A-C, Crijns A P, Ubbels J F, Niezink A G, Langendijk J A, Wijsman R and Both S 2020a Evaluation of interplay and organ motion effects by means of 4D dose reconstruction and accumulation *Radiother. Oncol.* **150** 268–74
- Meijers A et al 2020b Assessment of range uncertainty in lung-like tissue using a porcine lung phantom and proton radiography *Phys. Med. Biol.* **65** 15155014
- Mory C, Janssens G and Rit S 2016 Motion-aware temporal regularization for improved 4D cone-beam computed tomography *Phys. Med. Biol.* **61** 6856–77
- Nakajima K et al 2018 Clinical outcomes of image-guided proton therapy for histologically confirmed stage I non-small cell lung cancer *Radiat. Oncol.* **13** 199
- Niepel S et al 2019 Feasibility of 4DCBCT-based proton dose calculation: an *ex vivo* porcine lung phantom study *Z. Med. Phys.* **29** 249–61
- Niu T, Sun M, Star-Lack J, Gao H, Fan Q and Zhu L 2010 Shading correction for on-board cone-beam CT in radiation therapy using planning MDCT images *Med. Phys.* **37** 5395–406
- Paganetti H, Niemierko A, Ancukiewicz M, Gerweck L E, Goitein M, Loeffler J S and Suit H D 2002 Relative biological effectiveness (RBE) values for proton beam therapy *Int. J. Radiat. Oncol., Biol., Phys.* **53** 407–21
- Park Y-K, Sharp G C, Phillips J and Winey B A 2015 Proton dose calculation on scatter-corrected CBCT image: Feasibility study for adaptive proton therapy *Med. Phys.* **42** 4449–59
- Peroni M, Ciardo D, Spadea M F, Riboldi M, Comi S, Alterio D, Baroni G and Orecchia R 2012 Automatic segmentation and online virtualCT in head-and-neck adaptive radiation therapy *Int. J. Radiat. Oncol., Biol., Phys.* **84** e427–33
- Poludniowski G, Evans P M, Kavanagh A and Webb S 2011 Removal and effects of scatter-glare in cone-beam CT with an amorphous-silicon flat-panel detector *Phys. Med. Biol.* **56** 1837–51
- Rabe M et al 2021 Porcine lung phantom-based validation of estimated 4D-MRI using orthogonal cine imaging for low-field MR-linacs *Phys. Med. Biol.* **66** 5055006
- Ribeiro C et al 2021 Towards the clinical implementation of intensity-modulated proton therapy for thoracic indications with moderate motion: robust optimised plan evaluation by means of patient and machine specific information *Radiother. Oncol.* **157** 210–8

- Rit S, Clackdoyle R, Keuschnigg P and Steininger P 2016 Filtered-backprojection reconstruction for a cone-beam computed tomography scanner with independent source and detector rotations *Med. Phys.* **43** 2344–2352
- Rit S, Oliva M V, Brousmiche S, Labarbe R, Sarrut D and Sharp G C 2014 The reconstruction toolkit (RTK), an open-source cone-beam CT reconstruction toolkit based on the insight toolkit (ITK) *J. Phys. Conf. Ser.* **489** 012079
- Shrestha D, Tsai M-Y, Qin N, Zhang Y, Jia X and Wang J 2019 Dosimetric evaluation of 4D-CBCT reconstructed by simultaneous motion estimation and image reconstruction (SMEIR) for carbon ion therapy of lung cancer *Med. Phys.* **46** 4087–94
- Siewerdsen J H and Jaffray D A 1999 A ghost story: Spatio-temporal response characteristics of an indirect-detection flat-panel imager *Med. Phys.* **26** 1624–41
- Siewerdsen J H and Jaffray D A 2001 Cone-beam computed tomography with a flat-panel imager: Magnitude and effects of x-ray scatter *Med. Phys.* **28** 220–31
- Thing R S, Bernchou U, Mainegra-Hing E, Hansen O and Brink C 2016 Hounsfield unit recovery in clinical cone beam CT images of the thorax acquired for image guided radiation therapy *Phys. Med. Biol.* **61** 5781–802
- Thummerer A et al 2020 Comparison of the suitability of CBCT- and MR-based synthetic CTs for daily adaptive proton therapy in head and neck patients *Phys. Med. Biol.* **65** 23235036
- Tseng Y D, Wootton L, Nyflot M, Apisarnthanarax S, Rengan R, Bloch C, Sandison G and James S S 2018 4D computed tomography scans for conformal thoracic treatment planning: is a single scan sufficient to capture thoracic tumor motion? *Phys. Med. Biol.* **63** 202NT03
- Veiga C et al 2016 First clinical investigation of cone beam computed tomography and deformable registration for adaptive proton therapy for lung cancer *Int. J. Radiat. Oncol., Biol., Phys.* **95** 549–59
- Verma V, Lin S H, Simone C B and Mehta M P 2016 Clinical outcomes and toxicities of proton radiotherapy for gastrointestinal neoplasms: a systematic review *J. Gastrointestinal Oncol.* **7** 644–64
- Wang P et al 2016 Quantitative assessment of anatomical change using a virtual proton depth radiograph for adaptive head and neck proton therapy *J. Appl. Clin. Med. Phys.* **17** 427–40
- Weber D C, Schneider R, Goitein G, Koch T, Ares C, Geismar J H, Schertler A, Bolsi A and Hug E B 2012 Spot scanning-based proton therapy for intracranial meningioma: Long-term results from the Paul Scherrer Institute *Int. J. Radiat. Oncol., Biol., Phys.* **83** 865–71
- Welsh J et al 2011 Intensity-modulated proton therapy further reduces normal tissue exposure during definitive therapy for locally advanced distal esophageal tumors: a dosimetric study *Int. J. Radiat. Oncol., Biol., Phys.* **81** 1336–42
- Wolthaus J W H, Sonke J-J, van Herk M and Damen E M F 2008a Reconstruction of a time-averaged midposition CT scan for radiotherapy planning of lung cancer patients using deformable registration *Med. Phys.* **35** 3998–4011
- Wolthaus J W, Sonke J-J, van Herk M, Belderbos J S, Rossi M M, Lebesque J V and Damen E M 2008b Comparison of different strategies to use four-dimensional computed tomography in treatment planning for lung cancer patients *Int. J. Radiat. Oncol., Biol., Phys.* **70** 1229–38
- Zhang Y, Yin F-F and Ren L 2015 Dosimetric verification of lung cancer treatment using the CBCTs estimated from limited-angle on-board projections *Med. Phys.* **42** 4783–95
- Zijp L, Sonke J-J and van Herk M 2004 Extraction of the respiratory signal from sequential thorax cone-beam x-ray images 2004 *Int. Conf. on the Use of Computers in Radiation Therapy* pp 507–9
- Zöllner C, Rit S, Kurz C, Vilches-Freixas G, Kamp F, Dedes G, Belka C, Parodi K and Landry G 2017 Decomposing a prior-CT-based cone-beam CT projection correction algorithm into scatter and beam hardening components *Phys. Imaging Radiat. Oncol.* **3** 49–52